Magn Reson Med Sci, Vol. 5, No. 2, pp. 79–88, 2006

MAJOR PAPER

Evaluation of RF Heating on Humerus Implant in Phantoms during 1.5T MR Imaging and Comparisons with Electromagnetic Simulation

Hiroyuki MURANAKA[1,2*], Takayoshi HORIGUCHI[1], Shuji USUI[1], Yoshitake UEDA[1], Osamu NAKAMURA[3,4], Fumiaki IKEDA[5], Ken IWAKURA[5], and Giichirou NAKAYA[6]

[1]*Major in Medical Engineering and Technology, Graduate Course in Integrated Human Sciences Studies, Hiroshima International University 555-36 Kurose-Gakuendai, Higashi-Hiroshima 724-0695, Japan*
[2]*Department of Radiology, Hiroshima Prefectural Rehabilitation Center*
[3]*ING Co., Ltd.*
[4]*Chuoh College of Medical Technology*
[5]*PHOTON Co., Ltd.*
[6]*Josai College of Medical Arts and Sciences*
(Received March 31, 2006; Accepted July 5, 2006)

Purpose: To evaluate the effect of radiofrequency (RF) heating on a metallic implant during magnetic resonance imaging (MRI), temperatures at several positions of an implant were measured, and results are compared with electromagnetic simulations using a finite element method.

Methods: A humerus nail implant made of stainless steel was embedded at various depths of tissue-equivalent gel-phantoms with loop (loop phantom) and partially cut loop (loop-cut phantom), and the phantoms were placed parallel to the static magnetic field of a 1.5T MRI device. Scans were conducted at maximum RF for 15 min, and temperatures were recorded with 2 RF-transparent fiberoptic sensors. Finally, electromagnetic-field analysis was performed.

Results: Temperatures increased at both ends of the implants at various depths, and temperature increase was suppressed with increasing depth. The maximum temperature rise was 12.3°C at the tip of the implant and decreased for the loop-cut phantom. These tendencies resembled the results of electromagnetic simulations.

Conclusion: RF heating was verified even in a nonmagnetizing metal implant in a case of excessive RF irradiation. Particularly, rapid temperature rise was observed at both ends of the implant having large curvatures. The difference in temperature increase by depth was found to reflect the skin-depth effect of RF intensity. Electromagnetic simulation was extremely useful for visualizing the eddy currents within the loop and loop-cut phantoms and for evaluating RF heating of a metallic implant for MRI safety.

Keywords: *magnetic resonance imaging, metallic implant, RF heating, electromagnetic simulation, MRI safety*

Introduction

Magnetic resonance (MR) imaging is an important modality, with no ionizing radiation exposure, and it is used daily for clinical diagnosis in many rehabilitation facilities. During MR imaging of implanted patients in such facilities, there is a risk of RF heating, and special attention must be paid to such cases. Research concerning implants in the human body has focused primarily on durability and biocompatibility, and research into their safe use in MR imaging is insufficient. However, the influence of RF heating of the implant on the human body during MR imaging has been examined,[1-14] and in most reports, the heating is small.[1-9]

*Corresponding author, Phone: +81-82-425-1455, Fax: +81-82-425-1094, E-mail: muranaka@rehab-hiroshima.gr.jp

RF heating is attributed mainly to electric currents induced by RF irradiation and switching of a gradient magnetic field. However, Shellock[15] reports that induced current from switching can be disregarded and that RF irradiation is the main factor affecting heating. Rapid increase in the temperature of an implant in the human body may cause pain. We have examined the mechanism of RF heating in a preliminary experiment using various metal balls[10] and confirmed Shellock's result. Moreover, RF heating at the surface of nonmagnetizing metal balls has been verified. RF heating of implanted spinal fusion stimulators,[11] neurostimulation systems for deep brain stimulation,[12] and cardiac pacemakers and electrodes[13] have been reported.

As described in these reports, generation of induced current seems to involve the loop formation.[14,16] In addition, there are some reports of burn accidents caused by the loop formation during MR procedures.[17–19] Extra caution is still needed when an implant is in the loop. Although Shellock's group has made several reports concerning MRI safety, a definitive guideline about MR procedure in an implanted patient has not been published.[15,20–22] Moreover, because the performance and pulse sequences of MR equipment are now different from those at that time, such risk is now greater. We have experienced several cases in which implanted patients reported pain and MR procedures were stopped.

The mechanism of heat generation by RF irradiation in the human body is complicated. RF heating of an implant in a patient is influenced by the quality of material and shape of the implant, body shape, electrical properties of various internal organs, thermoregulatory reaction, blood flow, and other parameters. Therefore, we have embedded a humerus nail implant in tissue-equivalent phantoms to verify RF heating and identify where it occurs. The influences of depth of embedded implant from the phantom surface and of the loop formation are also examined in detail. Furthermore, we performed electromagnetic simulation of RF heating and compared our findings with the experimental results.

Methods

Phantom and implant

The tissue-equivalent phantom supposing human upper limbs was made according to the modified procedure of Kato and associates.[23] For the phantom, powdery gelatinizer with 9% carrageenan (Cool Agar, Nitta Gelatin Inc.) was melted in distilled water, and a small amount of salt (0.19 w%) was mixed in to adjust the electrical property to be equivalent to that of muscular tissue. The vessel was prepared by arranging an acrylic box measuring 42 cm long by 10 cm wide in the center of a polypropylene container 67 cm long by 35 cm wide (Fig. 1a). Semisolid gel was added to a depth of 14 cm between the empty acrylic box and the outer container to form a loop (total weight, about 30 kg; Fig. 1c [loop phantom]). The perimeter of the loop is nearly equal to 1/4 wave length ($1/4 \times 4.7$ m) for the resonance frequency on a 1.5T MRI device. Another phantom was prepared to simulate loop-cutting effect. One side of the phantom was cut by 2.5 cm, supposing that hands do not touch (Fig. 1b [loop-cut phantom]).

The implant was a 24-cm-long MD/N humerus nail (Zimmer Inc.) made of stainless steel (Austenitic grade, ASTM F138) and used to treat fractures. The implant was embedded parallel with the direction of a static magnetic field. The position of the implant was varied simultaneously by depth and distance from the container wall (Figs. 1c, d) so that both the depth and the distance were set at the same value D to equalize the effect of RF irradiation.

MRI exposure

All examinations were performed with a 1.5T MR scanner (MAGNETOM Symphony, SIEMENS). Maximum RF-heating condition was achieved using the following setting parameters. Scan plane, coronal; pulse sequence, HASTE (half Fourier acquisition single-shot turbo spin echo); echo time, 248 ms; repetition time, 1030 ms; field of view, 50 cm; slice thickness, 5 mm; matrix, 256 $\times$256; number of excitations, 32; number of slices, 25; number of echoes, 256; presaturation pulse, parallel-AP; and scan time, 15 min. The transmit/receive body coil was used. The console-predicted, whole-body averaged specific absorption ratio (SAR) was about 4.0 W/kg for these settings and a body weight of 30 kg, using body coil at the maximum in first-level management operation mode. The transmit/receive body coil contained 4 exposure coils (35×70 cm) constituting 2 pairs of opposite coils for 90° phase-shifted exposure. To attain maximum SAR, the output gain of RF power was adjusted manually. Moreover, the power supply of the gradient magnetic field was set in off-mode.

Temperature measurements

Two fiberoptic FL-2000 thermometers (Anritsu Keiki Inc.) were used to measure temperature. The thermometers were composed of optical fibers measuring 10 m long and were not influenced by magnetic field and RF irradiation. These fiberoptic

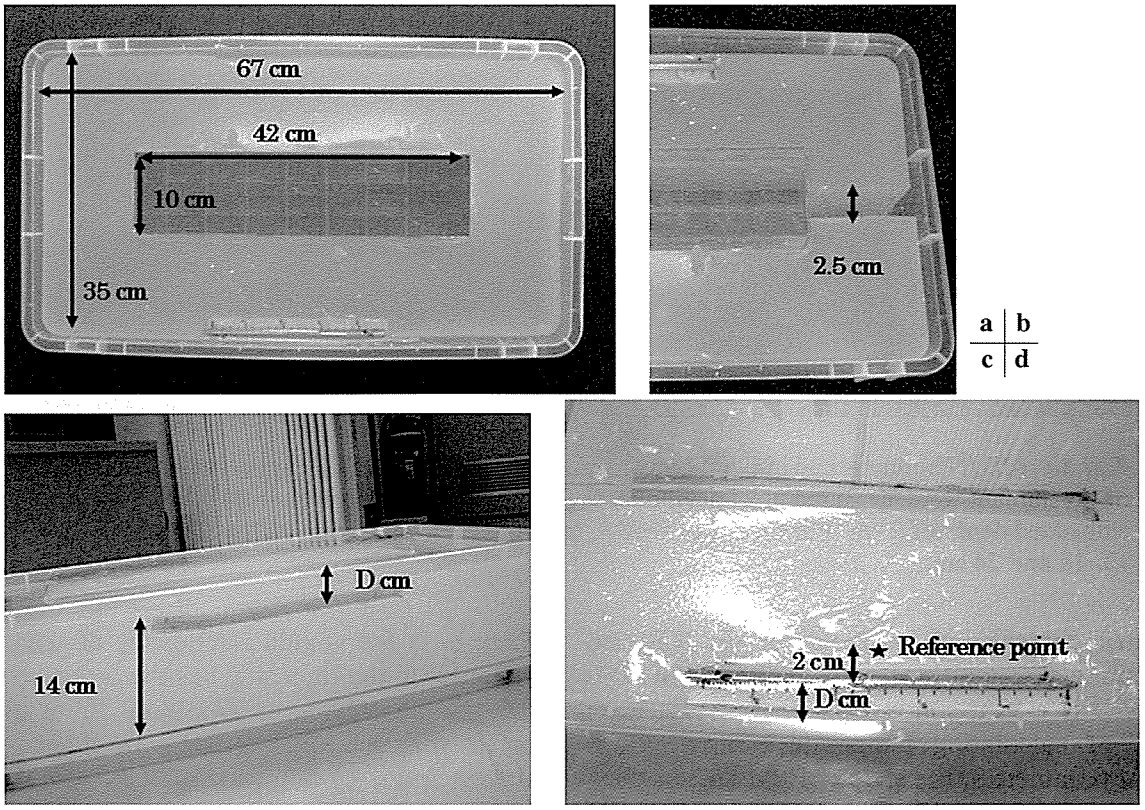

Fig. 1. Dimensions of tissue-equivalent phantoms
a: Loop phantom. The outer side is made of a polypropylene container with dimensions 35 × 67 cm, and the inner side is made of an acrylic box with dimensions 10 × 42 cm. Powdery gelatinizer (Cool Agar) was melted in distilled water, and the electrical property was approximated to muscular tissue. Total weight is 30 kg.
b: Loop-cut phantom. The central part of one side 35 cm in length was cut by 2.5 cm.
c: Semisolid gel was filled to a depth of 14 cm, and an implant was embedded at a depth of D [cm] from the surface.
d: The distance between the implant and the outer container edge is also D [cm]. The implant was embedded parallel with a static magnetic field. The position of the implant is varied simultaneously by the depth D and distance D to equalize the effect of RF irradiation.

sensors were absolutely calibrated with the thermocouple thermometer. Temperatures of the implant surface were measured at 24 positions, each with 1-cm separation from the tip to the base, for an embedded depth of 2 cm. For the other depths, temperatures were measured at 6 positions–at 0, 2, 6, 12, 18 and 24 cm (Fig. 2).

The reference point for temperature measurement was 2 cm from the surface of the center of the implant (Fig. 1d). Actual temperature increase was evaluated as the difference of the temperatures between the reference and measuring points because of the gradual rise in the whole phantom from the large number of measurements. The temperatures were recorded by 1-s intervals from 1 min before 15-min RF irradiation to 10 min after the RF irradiation. The temperature of the MR scanning room was kept in advance at 24°C, and the phantom was left in the room more than 4 hours prior to the experiment to equalize its temperature with that of the room. All measurements were performed 3 times, and the averaged value was estimated to be the experimental temperature.

Electromagnetic-field analysis

RF heating of the implant and the phantom was analyzed with pre and post processor Femap (UGS Co., Ltd.) and PHOTO-EDDY$j\omega$ and PHOTO-THERMO software (PHOTON Co., Ltd.), which are all based on the finite element method. The electric current of the RF-irradiation coils was calculated from the RF power displayed on the MR console and the known resistance of the coils.

PHOTO-EDDY$j\omega$ is a static- and transient-field analysis software capable of calculating eddy current. The electric current density and amount of heating from Joule loss can also be calculated with this software. As input parameters, the shape of the object, specific permeability, electrical conductivi-

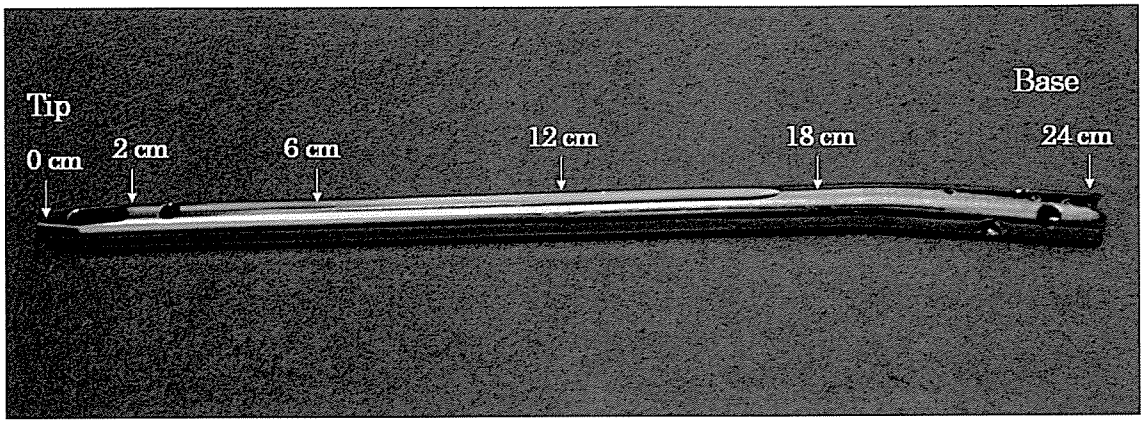

Fig. 2. MD/N humerus nail implant (Austenitic grade, ASTM F138, Zimmer Inc.). Temperatures of the implant were measured at 24 positions, each 1-cm separation from the tip to the base, for an embedded depth of 2 cm. For the other depths, temperatures were measured at 6 positions–0, 2, 6, 12, 18 and 24 cm.

ty, electric current and frequency of the RF, and the boundary conditions are given. PHOTO-THERMO is a heat-conduction analysis software capable of calculating temperature distribution. As input parameters, the shape of the object, thermal conductivity, specific heat, mass density, and boundary conditions are given.

Theory of electromagnetic-field analysis

Maxwell's equations for the electromagnetic field are described with differential operator (∇) as follows:

$$\nabla\cdot\mathbf{D}=\rho,\quad \nabla\times\mathbf{E}=-\partial\mathbf{B}/\partial t,\quad \nabla\cdot\mathbf{B}=0,$$
$$\nabla\times\mathbf{H}=\mathbf{J}+\partial\mathbf{D}/\partial t, \tag{1}$$

where there are relations of $\mathbf{D}=\varepsilon\mathbf{E}$ (ε: dielectric constant) between electric displacement $\mathbf{D}$ and electric field $\mathbf{E}$, and $\mathbf{B}=\mu\mathbf{H}$ (μ: permeability) between magnetic flux density $\mathbf{B}$ and magnetic field $\mathbf{H}$. Also, ρ is electric charge density, and $\mathbf{J}$ is electric current density. Here, by introducing vector potential $\mathbf{A}$, $\mathbf{B}$ and $\mathbf{E}$ are expressed under an appropriate gauge as follows:

$$\mathbf{B}=\nabla\times\mathbf{A},\quad \mathbf{E}=-\partial\mathbf{A}/\partial t. \tag{2}$$

Current density $\mathbf{J}$ is divided into input current ($\mathbf{J}_0$) and induced eddy current and is expressed as $\mathbf{J}=\mathbf{J}_0+\sigma\mathbf{E}$ (σ is electrical conductivity) by applying Ohm's law for the latter current.

In cases of RF irradiation of a human body or a phantom, the current consists of only induced eddy current because $\mathbf{J}_0=0$. The following equation is derived by substituting Eq. (2) for the last equation of (1),

$$\nabla\times\mu^{-1}\nabla\times\mathbf{A}=-\sigma\partial\mathbf{A}/\partial t+\varepsilon\partial^2\mathbf{A}/\partial t^2. \tag{3}$$

Here, the magnitude of each term on the right side in Eq. (3) is estimated by putting $\mathbf{A}=\mathbf{A}_0\sin\omega t$, where ω is the angular frequency of the RF. The first term on the right side has the order of $O(\sigma\omega\mathbf{A})$ and the second term $O(\varepsilon\omega^2\mathbf{A})$. It is generally correct that $\sigma\approx10^6$ S/m for a conductor like the implant and $\sigma\leq1$ S/m, $\varepsilon\approx10^{-12}$ F/m for the semi-solid gel inside the phantom. Therefore, the first term becomes relatively large in the conductor, and the second term becomes relatively large inside the phantom for $\omega=2\pi f$ ($f\approx100$ MHz$=10^8$ Hz).

In the PHOTO-EDDYjω software, sinusoidal oscillation is assumed for the temporal field variation. Then, it is possible to define the field, $\mathbf{A}(x, y, z, t)$, which satisfies Eq. (3) as follows:

$$\mathbf{A}(x, y, z, t)\equiv\mathrm{Re}(\mathbf{A}_C(x, y, z)\exp(j\omega t)), \tag{4}$$

where the complex field $\mathbf{A}_C(x, y, z)$ is introduced, and Re means the operation to take the real part of the complex number. Because this operation and space and/or time differentiations are permutable, Eq. (3) is expressed as follows:

$$\nabla\times\mu^{-1}\nabla\times\mathbf{A}=-j\omega\sigma\mathbf{A}+\varepsilon\omega^2\mathbf{A}. \tag{5}$$

In PHOTO-EDDYjω, this complex field (real and imaginary parts) can be obtained as analyzed results. Actual field at an arbitrary time can be described from definition (4) as

$$\mathbf{A}(x, y, z, t)=\mathrm{Re}(\mathbf{A}_C(x, y, z))\cos\omega t - \mathrm{Im}(\mathbf{A}_C(x, y, z))\sin\omega t,$$

so it is obtained from the complex field. Also from the above consideration, it is possible to interpret the real part of the complex field as the field at $t=0$ and the imaginary part as that at $t=-\pi/2\omega$ (phase advances by 90°). In the electromagnetic-field analysis, the inside of the phantom including the implant is divided into many minute meshes with pre and post processor Femap. Next, the vector

Table. The physical properties of materials required for electromagnetic analysis

Physical property	Phantom	Implant
Mass density ρ_m (kg/m^3)	542.7	7073.6
Specific permeability μ_r	1.00	1.02
Electrical conductivity σ (S/m)	0.769	1.35×10^6
Specific heat C (J/K·kg)	3.63×10^3	5.00×10^2
Thermal conductivity κ (W/m·K)	0.55	16.20

potential **A** is obtained for each mesh with PHOTO-EDDYjω; then **B**, **E** and eddy current σ**E** are evaluated.

Thereafter, based on the generated amount of heat, the heat-conduction equation is solved with the PHOTO-THERMO software, and temperature distribution is evaluated. The outline is described in the following. In general substances, there is a relationship of $\mathbf{q}=-\kappa\nabla T$ between thermal flux **q**, that is, energy flow passing through unit area per unit time and temperature T, where κ is thermal conductivity. In addition, the internal energy u, which a substance has in unit mass, is expressed as $u=CT$, where C is specific heat. From these relations and the energy conservation law, the fundamental equation for the heat conduction is expressed as

$$\rho_m C\cdot\partial T/\partial t-\nabla\cdot(\kappa\nabla T)=Q,$$

where ρ_m is mass density and Q is an amount of heating in unit volume. In PHOTO-THERMO, steady-state analysis and transient analysis can be performed with this basic equation.

The mass densities (ρ_m), specific permeabilities (μ_r), electrical conductivities (σ), specific heats (C), and thermal conductivities (κ) of the phantom and the implant used in the present experiment are listed in the Table. These parameters are used for the electromagnetic-field analysis in this work. At first, to evaluate RF heating of the phantom and the implant, these are divided into small meshes with Femap, considering the attenuation rate of RF power from outer-skin effect. Particularly, meshes in the tip of the implant and nearby phantom are made smaller with a 3D model, and the total number of meshes is 36000. This model reproduces considerably well the actual shapes of the present implant and phantoms. Four RF-irradiation coils have the same size as previously mentioned and are reproduced as pairs of opposite coils inside the gantry in the simulation.

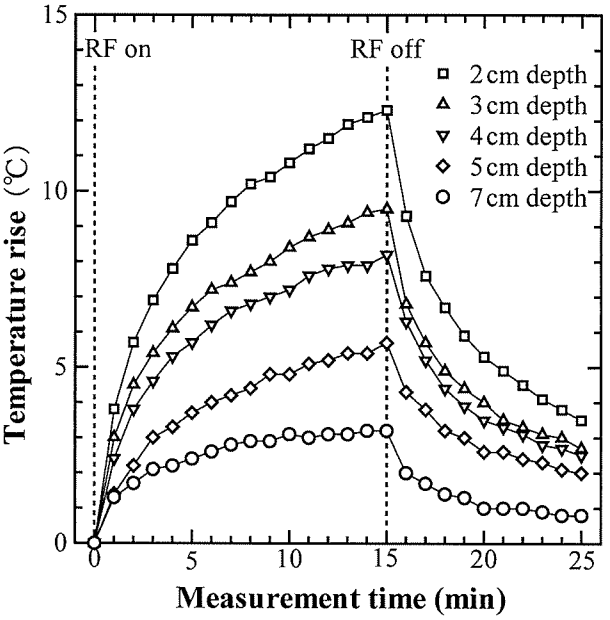

Fig. 3. Temporal temperature changes of the tip of the implant. Measurement duration was 1, 15 and 10 min before, during and after RF irradiation, respectively. The depth from the phantom surface was also changed as a parameter (2, 3, 4, 5 and 7 cm).

Results

Temporal temperature change

Temporal temperature changes of the tip of the implant are shown in Fig. 3, where embedding depths from the phantom surface are also varied. The temperature rise of the reference point in the phantom was 0.5°C or less during RF exposure. As the figure shows, the temperature rose gradually with RF on and decreased rapidly with RF off. As the embedding depth diminishes, the temperature increases more rapidly. The maximum temperature rise reached 12.3°C at 15 min after RF was on for the minimum depth of 2 cm.

Spatial temperature change

After 15 min of RF on, temperature rise is shown in Fig. 4 for the distance from the tip of the implant, where embedding depths are also varied. Measured points are 24 for 2-cm depth and 6 for

the other depths. Generally, the temperature increases at both ends were larger than those of central parts for all depths. Especially, the maximum rises were observed at the tip for all depths. Moreover, it is found from the figure that the difference of the maximum increases was small between 2-cm and 3-cm depths and increased as depth increased. The maximum rise for 7-cm depth, which corresponds to the skin depth of RF power, was less than one-third compared with that for 2-cm depth.

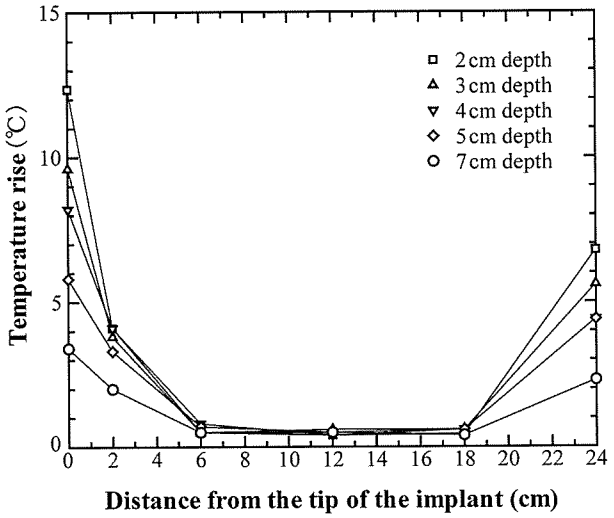

Fig. 4. Spatial temperature changes. After 15 min of RF on, the increase in temperature was measured for the distance from the tip of the implant and for various embedding depths. These measurements were carried out at 24 positions for 2-cm depth and 6 positions for the other depths.

Influence of loop cutting

Temporal temperature changes of the tip of the implant with and without loop cutting of the phantom are shown in Fig. 5a for 2-cm depth from the phantom surface. The temperature rise was clearly suppressed by loop cutting. The maximum rise for the loop-cut phantom was 9.1°C, which is smaller than the 12.3°C for the loop phantom. This corresponds to the value between 4-cm and 5-cm depths for the loop phantom. The temperature rises after RF on are compared between loop and loop-cut phantoms in Fig. 5b for the distance from the tip of the implant. Considerable differences were found at both ends of the implant, but no significant differences were recognized in the central part. To examine this result further, electromagnetic-field analysis was performed.

The eddy current map

The eddy current maps calculated with PHOTO-EDDY$j\omega$ are shown in Figs. 6a-d, where the unit of the current is A/m^2. The eddy current in the implant embedded in the loop phantom flows uniformly from the base to the tip (Fig. 6a). In contrast, in the loop-cut phantom, the eddy current circulates through the inside of the implant (Fig. 6b). The eddy current generated in the loop phantom is also large and flows toward the one-way direction. Moreover, the current is crowded near the surrounding of the implant (Fig. 6c). On the other hand, the eddy current in the loop-cut phantom is smaller than that in the loop phantom, and

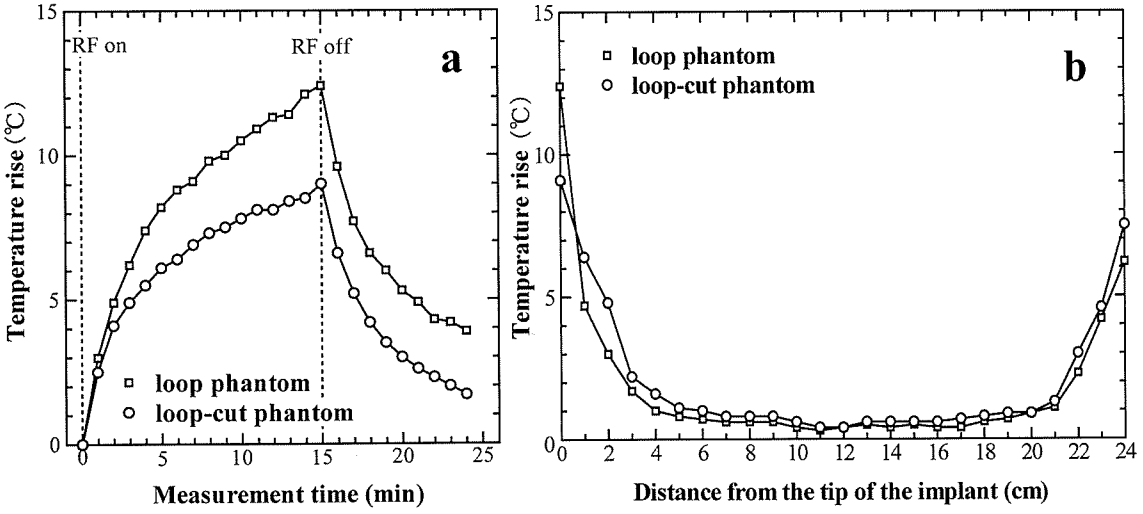

Fig. 5. Influence of loop cutting

a: Temporal temperature rises at the tip of the implant were measured for the phantoms with and without loop cutting for the embedding depth of 2 cm. Temperature increase was clearly suppressed by loop cutting.

b: Temperature increases after 15 min of RF on for the distance from the tip of the implant are compared between loop and loop-cut phantoms.

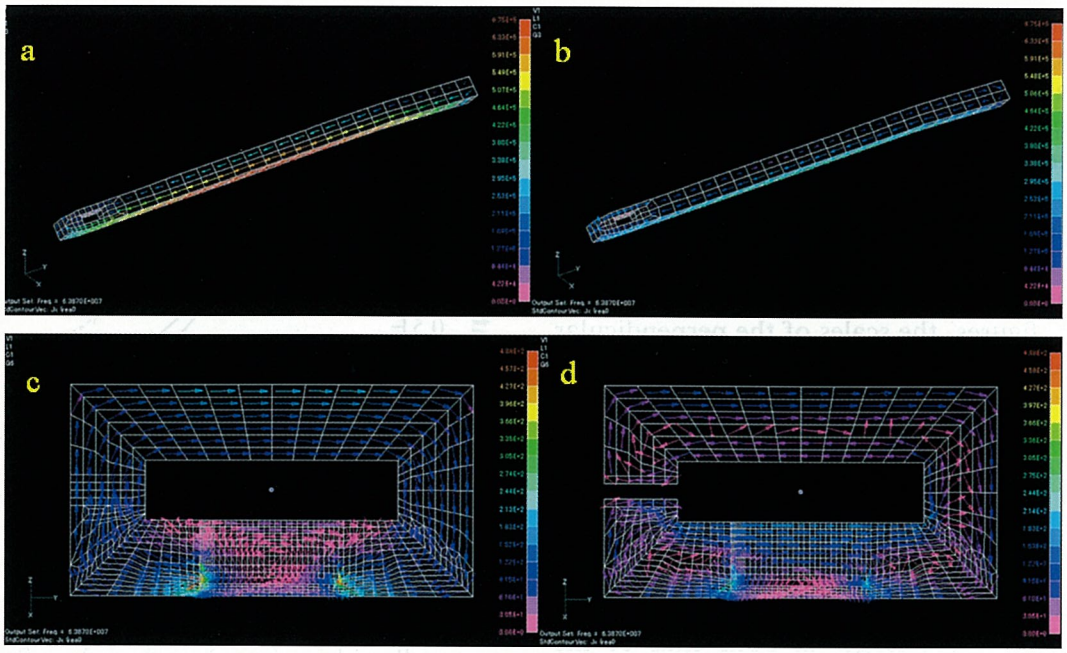

Fig. 6. The eddy current maps calculated with PHOTO-EDDYjω in the electromagnetic-field analysis. The unit of the current is A/m^2.
a: The implant in a loop phantom. The eddy current is flowing uniformly from the base to the tip.
b: The implant in a loop-cut phantom. The eddy current circulates through the inside of the implant.
c: The loop phantom. The eddy current is large and is flowing toward the one-way direction. It is crowded near the surrounding of the implant.
d: The loop-cut phantom. The eddy current is small and clearly not so crowded near the surrounding of the implant.

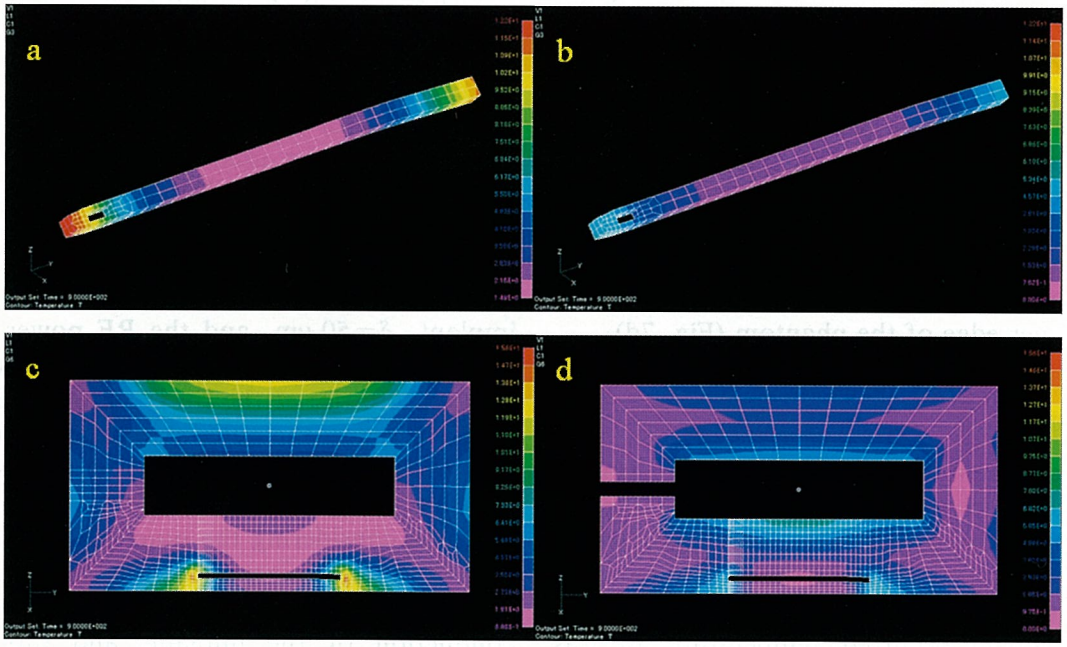

Fig. 7. The temperature maps calculated with PHOTO-THERMO in the electromagnetic-field analysis. The unit of the temperature is °C. Temperature maps were obtained after 15-min RF irradiation.
a: The implant in a loop phantom. Temperature increases are larger at both ends of the implant than those in the other parts. The maximum value is 12.2°C at the tip of the implant.
b: The implant in a loop-cut phantom. The tendency of temperature rise in the implant is similar to that in the loop phantom. The maximum value is 5.3°C.
c: The loop phantom. The temperature change is the largest near both ends of the implant, and considerable temperature rise is observed near the outer edge of the opposite side.
d: The loop-cut phantom. The temperature rise is relatively suppressed, but a little rise is observed in the inner edge of the phantom.

the current is clearly not so crowded near the surrounding of the implant (Fig. 6d). These eddy current maps were converted to RF-heating maps considering Joule loss with PHOTO-EDDYjω.

Temperature map

RF-heating maps were converted to temperature maps by solving heat-conduction equations with PHOTO-THERMO. Temperature maps obtained after 15-min RF irradiation are shown in Figs. 7a-d. In the figures, the scales of the perpendicular axes are described separately in the legends. The electric current flowing through each pair of coils was evaluated from the RF load (W) and the resistance of 50 Ω for the pair of coils. The averaged electric current was 4.6 A per unit coil in the present experiment. The parameters of the Table were input in the present analysis. It is generally found from Figs. 7a and b that the temperature rises are larger at both ends of the implant than those in the other parts also in the electromagnetic-field analysis. Especially, the maximum temperature rise was found at the tip of the implant in the loop phantom (Fig. 7a). The maximum value of 12.2°C was approximately the same as the measured value of 12.3°C.

On the other hand, the tendency of temperature rise in the implant embedded in the loop-cut phantom was similar to that in the loop phantom, but the maximum value was 5.3°C, which is low by 3.8°C compared with the measured value (Fig. 7b). The temperature change in the loop phantom was the largest near both ends of the implant, and considerable temperature rise was observed near the outer edge of the opposite side (Fig. 7c). General temperature rise in the loop-cut phantom was relatively suppressed, but a small increase was observed at the inner edge of the phantom (Fig. 7d).

Discussion

This experiment confirmed that RF heating occurs even in such a large nonmagnetizing implant by RF irradiation. Particularly, both ends where the implant was in contact with the phantom heated with irradiation. In the tip of the implant, where maximum heating occurred, temperature rise was larger closer to the phantom's surface, and the temperature changed rapidly. At depths of 2 and 3 cm from the phantom surface, the maximum temperature increases were not so different, and at over 5-cm depth, the rises were about half of those at 2-cm depth. The outer-skin depth of RF power (δ), which corresponds to the depth of 37% attenuation (that is, 1/e), can be estimated from magnetic permeability, electrical conductivity, and resonance

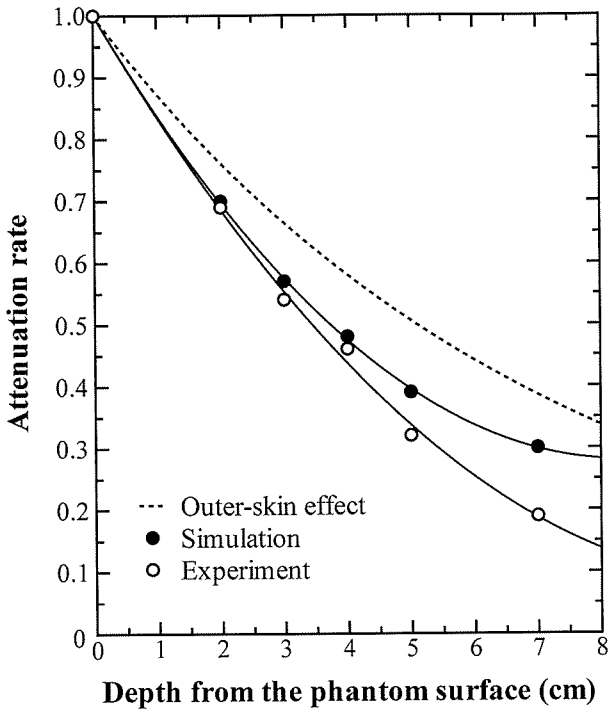

Fig. 8. The attenuation rate of temperature rise at the tip for the depth from the phantom surface. The attenuation rate is normalized at the depth of 0 cm. The outer-skin effect of RF power is represented by the dashed line. Experimental values are represented as open circles (○) and simulation value as closed circles (●). Solid lines are drawn to guide the eye.

frequency with the expression of $\delta=(\pi\mu\sigma f)^{-1/2}$. For the phantom used in this experiment, δ is estimated to be about 7.2 cm by substituting the values of $f=63.8$ MHz, $\sigma=0.769$ S/m and $\mu=\mu_r\cdot\mu_0=1.00\cdot4\pi\cdot10^{-7}$ N/A^2. On the other hand, because of $\sigma=1.35\cdot10^6$ S/m and $\mu=1.02\cdot\mu_0$ for the implant, $\delta=50\,\mu$m, and the RF power is almost attenuated at the surface. The attenuation rate of temperature rise at the tip is shown in Fig. 8 and seems to reflect the outer-skin effect. In the figure, both the experimental value (○) and the simulation value (●) decreased more rapidly than the calculated value considering the outer-skin effect (dashed line) as the depth increased. This fact is considered to be the influence of heat dissipation by the heat conduction of the implant, and this tendency appears more notably in the experimental value. The simulation value may approach the experimental value if the mesh size is made more minute.

As the static magnetic field becomes larger, the resonance frequency becomes higher. Consequently, the outer-skin depth is closer to the phantom surface. For example, the value is estimated to be about 4.5 cm for the magnetic field of 3T, and the danger of RF heating increases more as the

implant is closer to the skin surface of a human body. Conversely, it is thought that RF heating is not so large for the implant in a deeper position from the skin surface.

From these results, the risk of RF heating is predicted for the embedded implant even during usual MR imaging. That is, local heating may take place in a short period even in an implant as large as that in this study in a case of shallow embedding depth. This means that the shape of the implant has to be taken into consideration. Where curvature is large and surface area is small, temperature rise is high and the temperature change is rapid because of fast heat storage. This situation causes the increase of local SAR and leads to the so-called hot-spot formation. In contrast, the temperature rise is low with deeper embedding depth, and the risk of heating is decreased.

In the electromagnetic-field analysis, the places where the RF heating occurred in the simulation corresponded with those in the experiment, and the calculated temperature rises reproduced the measured values very well. On the other hand, it was found practicable to suppress the temperature rise of the tip part by cutting a part of the loop. However, as for quantification, the calculated temperature rises and measured values differed. Nevertheless, electromagnetic simulation is considered very useful for understanding the mechanism of heat generation because eddy current distributions are also obtained simultaneously in visible forms in the simulation.

In the loop phantom, the eddy current generated in the implant flows to a one-way direction, and the current flowing the periphery of the phantom is relatively large and uniform. Thus, when an implant was placed parallel with the direction of static magnetic field as in this study, the induced current was easily generated.[11,15] The generated induced current concentrated at the tip of the implant, just like an antenna (Fig. 6a). In addition, the current was strengthened by the loop formation. The eddy current distribution indicated that the current flowed densely near the periphery of the implant contacting with the phantom, which has different electrical properties (Fig. 6b). These results show that large temperature rises are caused by the large electrical resistance between the implant and the phantom. From a theoretical consideration, when current densities in the phantom and the implant are the same in the boundary region, it is concluded that heat generation increases in the phantom region having larger electrical resistance (Fig. 7c).

On the other hand, in the loop-cut phantom, the temperature map of the implant after 15-min RF irradiation is generally underestimated, and the inner phantom edge near the implant is slightly heated (Fig. 7d). The eddy current generated in the implant circulates inside, and the heating is consequently suppressed (Fig. 6c). Moreover, the current density distribution in the loop-cut phantom is clearly lower near the ends of the implant than that in the loop phantom (Figs. 6b, d). It is thought that heating of the inner phantom edge near the implant is caused by the forward eddy current and the backward current turned back from the cutting part of the loop. However, no significant heating was observed experimentally at the same position. Further experimental and theoretical verifications are required in this respect.

The results confirm the usefulness of the simulation with electromagnetic-field analysis. However, the human body is not composed of uniform tissue–it has various internal organs that have inherent electrical properties individually, and there are enormous blood vessels in the inside and periphery of the body. Blood flow has electrical conduction properties and has a cooling effect by heat transportation. Therefore, the present study using uniform phantoms provides a worst-case estimation. Moreover, implants are composed of various materials and have different sizes and shapes. Heat generation may be greatly affected by the angle between the implant and the static magnetic field. Concerning these subjects, we will perform further examinations.

Nevertheless, electromagnetic-field analysis is useful in predicting the heating by RF irradiation of the implant embedded in a human body because it enables simulation of the generation of eddy current and the temperature rises of the places where heating occurs. Although further examination will be required for the electromagnetic-field analysis, it may be an epoch-making technique for predicting the patient's risk during MR imaging.

Conclusion

In this research, the effect of RF heating was examined for the implant embedded in tissue-equivalent loop and loop-cut phantoms. Temperature increases were observed at both ends of a humerus nail implant embedded at various depths and placed parallel to the static magnetic field of a 1.5T MRI device. Maximum temperature rise was greater at shallower depth, reaching 12.3°C at the tip of the implant and decreasing for the loop-cut phantom. This result was found to reflect the skin-depth effect of RF intensity. Electromagnetic-field analysis showed that the generation of eddy current

by RF irradiation is relevant with loop formation, the heating of the implant is suppressed, and the eddy current distribution is changed by cutting a part of the loop. Although further examination is still required for safe MR imaging in clinical practice, the usefulness of electromagnetic-field analysis to simulate the heating effect of the implant was confirmed.

Acknowledgements

We wish to thank Zimmer Inc. for providing the humerus nail implant used in clinical practice. We also express our sincere thanks to Professor Shoogo Ueno, Department of Biomedical Engineering, Graduate School of Medicine, The University of Tokyo, for recommending that we contribute this study to MRMS.

References

1. Yamada M, Okada T, Kuwayama Y, Nakane M, Anno H. [Study of RF heat of dental magnetic keeper with 1.5-Tesla MR equipment.] Jpn J Radiol Technol 2000; 11:1371–1375. (Japanese with English abstract)
2. Nyehnuis JA, Kildishev AV, Bourland JD, Foster KS, Graber G. Heating near implanted medical devices by the MRI RF-magnetic field. IEEE Trans Magn 1999; 35:4133–4135.
3. Shellock FG, Morisoli SM. *Ex vivo* evaluation of ferromagnetism, heating, and artifacts produced by heart valve prosthesis exposed to a 1.5-T MR system. J Magn Reson Imaging 1994; 4:756–758.
4. Davis PL, Crooks L, Arakawa M, McRee R, Kaufman L, Margulis AR. Potential hazards in NMR imaging: heating effects of changing magnetic fields and RF fields on small metallic implants. AJR Am J Roentgenol 1981; 137:857–860.
5. Mark AS, Hricak H. Intrauterine contraceptive devices MR imaging. Radiology 1987; 162:311–314.
6. Bhidayasiri R, Bronstein JM, Sinha S, et al. Bilateral neurostimulation systems used for deep brain stimulation: *in vitro* study of MRI-related heating at 1.5 T and implications for clinical imaging of the brain. Magn Reson Imaging 2005; 23: 549–555.
7. Buchli R, Boesiger P, Meier D. Heating effects of metallic implants by MRI examinations. Magn Res Med 1988; 7:255–261.
8. Baker KB, Tkach JA, Nyenhuis JA, et al. Evaluation of specific absorption rate as a dosimeter of MRI-related implant heating. J Magn Reson Imaging 2004; 20:315–320.
9. Shellock FG, Cosendai G, Park SM, Nyenhuis JA. Implantable microstimulator: magnetic resonance safety at 1.5 Tesla. Invest Radiol 2004; 39:591–599.
10. Muranaka H, Nakamura O, Usui S, Ueda Y, Morikawa K. [Influence of implants on human body during MRI examinations: Fundamental experiment using metal balls.] Jpn J Radiol Technol 2005; 61:1014–1020. (Japanese with English abstract)
11. Chou CK, McDougall JA, Chan KW. RF heating of implanted spinal fusion stimulator during magnetic resonance imaging. IEEE Trans Biomed Eng 1997; 44: 367–373.
12. Rezai AR, Finelli D, Nyenhuis JA, et al. Neurostimulation systems for deep brain stimulation: *in vitro* evaluation of magnetic resonance imaging-related heating at 1.5 Tesla. J Magn Reson Imaging 2002; 15:241–250.
13. Achenbach S, Moshage W, Diem B, Bieberle T, Schibgilla V, Bachmann K. Effects of magnetic resonance imaging on cardiac pacemakers and electrodes. Am Heart J 1997; 134:467–473.
14. Armenean C, Perrin E, Armenean M, Beuf O, Pilleul F, Saint-Jalmes H. RF-induced temperature elevation along metallic wires in clinical magnetic resonance imaging: influence of diameter and length. Magn Reson Med 2004; 52:1200–1206.
15. Shellock FG. Radiofrequency energy-induced heating during MR procedures: a review. J Magn Reson Imaging 2000; 12:30–36.
16. Yamazaki M, Yamada E, Kondou S, Higashida M. [Study of a temperature rise in RF irradiation during MR imaging: Measurements of local temperature using a loop phantom.] Jpn J Radiol Technol 2005; 8:1125–1132. (Japanese with English abstract)
17. Shellock FG, Slimp GL. Severe burn of finger caused by using a pulse oximeter during MR imaging (letter). AJR Am J Roentgenol 1989; 153:1105.
18. Knopp MV, Essig M, Debus J, Zabel HJ, van Kaick G. Unusual burn of the lower extremities caused by a closed conducting loop in a patient at MR imaging. Radiology 1996; 200:572–575.
19. Okuda T, Asao C, Yoshimatsu S, Saito R, Sugahara T, Yamashita Y. [Thermal injuries in two patients at MR imaging.] Jpn J Magn Reson Med 2004; 24:88–91. (Japanese with English abstract)
20. Shellock FG, Crues JV. MR procedures: biologic effects, safety and patient care. Radiology 2004; 232:635–652.
21. Shellock FG, Kanal E. Magnetic resonance: bioeffects, safety and patient management. NewYork: Raven Press, 1994; 101–121.
22. Shellock FG, Crues JV. High-field-strength MR imaging and metallic biomedical implants: an *ex vivo* evaluation of deflection forces. AJR Am J Roentgenol 1988; 151:389–392.
23. Kato H, Kuroda M, Yoshimura K, et al. [An MRI phantom using carrageenan gel.] Jpn J Magn Reson Med 2000; 20:365–373. (Japanese with English abstract)